

RESEARCH ARTICLE

10.1002/2017JB015210

Key Points:

- The dynamic fragmentation characteristics of jointed rock blocks during rockslide-avalanches have been analyzed by discrete element method
- The force concentration at the bottom leads to high fragmentation intensity and momentum boosts, increasing the fragment runout distance
- The final size, shape, and spatial distribution of large fragments are closely related to the initial joint orientation and distribution

Supporting Information:

- Supporting Information S1
- Data Set S1
- Movie S1
- Movie S2
- Movie S3

Correspondence to:

T. Zhao,
zhaotao@scu.edu.cn

Citation:

Zhao, T., Crosta, G. B., Dattola, G., & Utili, S. (2018). Dynamic fragmentation of jointed rock blocks during rockslide-avalanches: Insights from discrete element analyses. *Journal of Geophysical Research: Solid Earth*, 123. <https://doi.org/10.1002/2017JB015210>

Received 8 NOV 2017

Accepted 7 MAR 2018

Accepted article online 12 MAR 2018

Dynamic Fragmentation of Jointed Rock Blocks During Rockslide-Avalanches: Insights From Discrete Element Analyses

Tao Zhao¹ , Giovanni Battista Crosta² , Giuseppe Dattola², and Stefano Utili³ 

¹State Key Laboratory of Hydraulics and Mountain River Engineering, College of Water Resource and Hydropower, Sichuan University, Chengdu, China, ²Department of Earth and Environmental Sciences, Università degli Studi di Milano Bicocca, Milan, Italy, ³School of Engineering, Newcastle University, Newcastle upon Tyne, UK

Abstract The dynamic fragmentation of jointed rock blocks during rockslide avalanches has been investigated by discrete element method simulations for a multiple arrangement of a rock block sliding over a simple slope geometry. The rock blocks are released along an inclined sliding plane and subsequently collide onto a flat horizontal plane at a sharp kink point. The contact force chains generated by the impact appear initially at the bottom frontal corner of the rock block and then propagate radially upward to the top rear part of the block. The jointed rock blocks exhibit evident contact force concentration and discontinuity of force wave propagation near the joint, associating with high energy dissipation of granular dynamics. The corresponding force wave propagation velocity can be less than 200 m/s, which is much smaller than that of an intact rock (1,316 m/s). The concentration of contact forces at the bottom leads to high rock fragmentation intensity and momentum boosts, facilitating the spreading of many fine fragments to the distal ends. However, the upper rock block exhibits very low rock fragmentation intensity but high energy dissipation due to intensive friction and damping, resulting in the deposition of large fragments near the slope toe. The size and shape of large fragments are closely related to the orientation and distribution of the block joints. The cumulative fragment size distribution can be well fitted by the Weibull's distribution function, with very gentle and steep curvatures at the fine and coarse size ranges, respectively. The numerical results of fragment size distribution can match well some experimental and field observations.

1. Introduction

Rock mass with preexisting fractures and joints can be fragmented readily at impact upon the slope/ground surface during rock avalanches (Turcotte, 1986). The generated rock fragments of various sizes can be scattered on the ground surface affecting a large area. These events are very dangerous as characterized by almost instantaneous collapse, followed by a spreading stage of dynamic rock mass disintegration (Crosta et al., 2007; De Blasio & Crosta, 2015; Erismann & Abele, 2001; Heim, 1882; Legros, 2002; Scheidegger, 1973). They can pose significant hazards to human lives, structures and infrastructures, and lifeline facilities worldwide due to their enormous energy release and high mobility, threatening populated areas located even far away from the slope source region (Crosta et al., 2005; Hermanns et al., 2013; Stoopes & Sheridan, 1992; Whitehouse & Griffiths, 1983; Zhou et al., 2013).

Rock avalanches are always associated with dynamic rock fragmentation (Davies & McSaveney, 1999; De Blasio & Crosta, 2015; Locat et al., 2006), together with high spreading velocities, long runouts, and energy release, affecting the overall mobility and destructive power of rock avalanches (Agliardi & Crosta, 2003; Perinotto et al., 2015; Ruiz-Carulla et al., 2017). The related research has been performed by means of field observations in real rock avalanche deposits (Crosta et al., 2007; Dunning, 2006; Locat et al., 2006; Strom, 2006) and physical and numerical modeling (Bowman et al., 2012; Giacomini et al., 2009; Haug et al., 2016; Imre et al., 2010; Zhao et al., 2017). During the dynamic fragmentation, cracks propagate within the rock mass under compressive or tensile loading, together with the transmission and reflection of stress waves at impact (Crosta et al., 2007; Thornton et al., 1996). According to Xu (2005), the fracturing probability of a solid particle, such as ice, rock, and concrete, is controlled by its size, with large particles being most susceptible to breakage, producing fine grains. This fragmentation pattern is related to the tensile strength, as large particles with high coordination numbers (i.e., the number of contacts per particle) generally have low strength (Jaeger, 1967; Palmer & Sanderson, 1991). For rock blocks exhibiting preexisting joints, fragmentation is ruled by

the joint characteristics of the rock mass (e.g., spacing, orientation, persistence, and aperture). At impact, the rock mass can either disaggregate along the preexisting discontinuities or break along freshly formed faces, as controlled by the initial joint sets, impact energy, ground stiffness, and rock strength (Ruiz-Carulla et al., 2017). The existence of joints within the rock mass interrupts the transmission of stress waves, with a large amount of energy being dissipated at the discontinuities. In addition, the high loading strain rate at impact can also affect the fragmentation pattern (e.g., fracturing stress, size and number of fragments) and mechanisms of energy dissipation (Grady, 1981; Grady & Kipp, 1985).

Rock avalanche deposits usually consist of coarse or poorly sorted and layered crushed rocks with a prevalence of matrix material (Crosta et al., 2007). Thus, the representative rock block size distribution measured at the source and deposit areas reflect the fragmentation process and the corresponding energy consumption (Crosta et al., 2007; Dunning, 2006; Locat et al., 2006). As stated by Sammis and Ben-Zion (2008), the rock fragment size is determined by a competition between crack nucleation and stress relaxation processes occurring during impact. By analyzing the fragment size distribution of rockfall deposits, Ruiz-Carulla et al. (2017) characterized the volume of fragment by a three-parameter rockfall fractal fragmentation model. In their study, the discontinuity pattern of the detached rock mass is simulated by a discrete fracture network. In addition, the proportion of rock blocks still unbroken after the impact is expressed as a survival rate. The resultant distribution of rock fragments is well fitted by a power law function. From the fragment size analyses of the 1987 Val Pola rock avalanche, Crosta et al. (2007) concluded that a Weibull distribution can fit only a small part of the distribution, whereas a fractal distribution can fit a wider range of fragment sizes. They also concluded that multiple fragmentation processes took place during the rock avalanche motion, in which 1–30% of the initial potential energy was consumed. For rock fragmented by various processes (e.g., weathering, explosions, and impacts), the frequency-mass distribution of fragments fits well the fractal condition, indicating that fragmentation mechanisms are scale invariant (Turcotte, 1986).

Notwithstanding these advancements, a thorough understanding of the physical processes responsible for rock avalanche motion and dynamic fragmentation is still needed. In recent studies, Bowman et al. (2012), Bowman and Take (2015), and Haug et al. (2016) investigated the fragmentation of a small brittle block, sliding along an inclined plane, against a slope break. These studies have been considered as reasonable initial proxies to study rock fragmentation and propagation (De Blasio & Crosta, 2015). The current study considers this setting for numerical simulations by the discrete element method (DEM) (Cundall & Strack, 1979). The DEM has been widely employed as a tool for numerical modelling of rock avalanches and solid breakages (Boon et al., 2014, 2015b; Calvetti et al., 2000; Fu et al., 2017; Shen et al., 2017; Taboada & Estrada, 2009; Timár et al., 2012; Zhao et al., 2014, 2016, 2017). As stated by Alassi and Holt (2012), the method is capable of modeling complex dynamic responses of rock mass, such as crack initiation and propagation. The primary aim of this study is to investigate the fragmentation characteristics of jointed rock blocks subject to a single impact, and the subsequent debris spreading. The paper is organized as follows: section 2 illustrates the DEM model configuration of rock avalanche. Then, in section 3, the obtained numerical results are presented. Section 4 discusses some issues of rock fragmentation, such as momentum boost effect of fragment spreading, internal rock damage, fragment runout, and model size effect. Finally, conclusions on the capability of DEM in modelling dynamic fragmentation of jointed rock blocks are provided in section 5.

2. DEM Model Configurations of Rock Avalanche Simulation

The current study uses the open source DEM code ESyS-Particle (Weatherley et al., 2011) to run all simulations presented herein. The basic numerical algorithms of the bond model and of the linear elastic spring-dashpot contact model have been presented and calibrated in Zhao et al. (2017) on the basis of available experimental results of unconfined uniaxial compression and Split-Hopkinson Pressure Bar tests on coal rocks (Liu et al., 2015). The calibrated coal rock sample exhibits a bulk Young's modulus (E_b) of 1.67 GPa and uniaxial compression strength of 9.8 MPa. In the numerical model, the 3-D formulation of the bond breakage constitutive law proposed by Wang and Alonso-Marroquin (2009) has been employed in the simulations to determine whether rock damage occurs:

$$\frac{|F_{bn}|}{F_{bnMax}} + \frac{|F_{bs}|}{F_{bsMax}} + \frac{|M_b|}{M_{bMax}} + \frac{|M_t|}{M_{tMax}} \geq 1 \quad (1)$$

Table 1
Input Parameters of Rock Avalanche Simulations

DEM parameters	Value	DEM parameters	Value
Particle radius, r (mm)	0.75–2.25	Bond Young's modulus, E_b (GPa)	1.25
Particle density, ρ (kg/m^3)	2,650	Bond cohesion, c (MPa)	14.25
Particle friction angle, φ (deg)	30	Gravitational acceleration, g (m/s^2)	1962
Particle Young's modulus, E (GPa)	5	Viscous damping coefficient, β	0.01
Particle Poisson ratio, ν	0.25	DEM time step, Δt (s)	10^{-7}

Note. DEM = discrete element method.

where F_{bn} and F_{bs} are the normal and shear bonding forces; M_b and M_t are the bending and twisting torques, respectively; F_{bnMax} , F_{bsMax} , M_{bMax} and M_{tMax} are the threshold values of normal, shear, bending, and twisting strengths of the inter-particle bond, respectively. In addition, the viscous damping force (proportional to the relative velocity of particles in contact) has been adopted in the linear elastic spring-dashpot contact model. This parameter is employed to account for the energy dissipation and plastic deformations of the contacting particles occurring in the vicinity of the contact points.

These numerical models will be used in the current analyses, and the input DEM parameters are set the same as those listed in Zhao et al. (2017) (see also Table 1). In this study, the numerical simulations will be compared with the experimental work by Bowman et al. (2012), in which the coal rock was used as an analogue to typical rocks involved in rock avalanches due to its brittle and deliberately weak structure. A schematic view of the geometrical conditions of the rock avalanche model with a steep inclined sliding plane and a flat horizontal plane connected by a sharp break is shown in Figure 1. The sliding plane has a confined boundary condition, with its width being slightly larger than the granular block. The sliding slope channel has an inclination angle of 70° and height (H) of 425 mm. The slope channel is set frictionless, while the horizontal floor is made of a layer of fixed particles of uniform size 4.5 mm diameter to mimic a rough and bumpy ground (Jing et al., 2016; Utili et al., 2015). During the tests, the rock block is initially placed at the top of the slope and then released suddenly to slide downward under gravity. The magnitude of gravitational acceleration is set as $1,962 \text{ m/s}^2$ (200 g) to mimic centrifuge loading conditions, so that the stress and strain states of a small-scale model can approximately match those of real rock avalanches. It should be noted that the augmented gravity

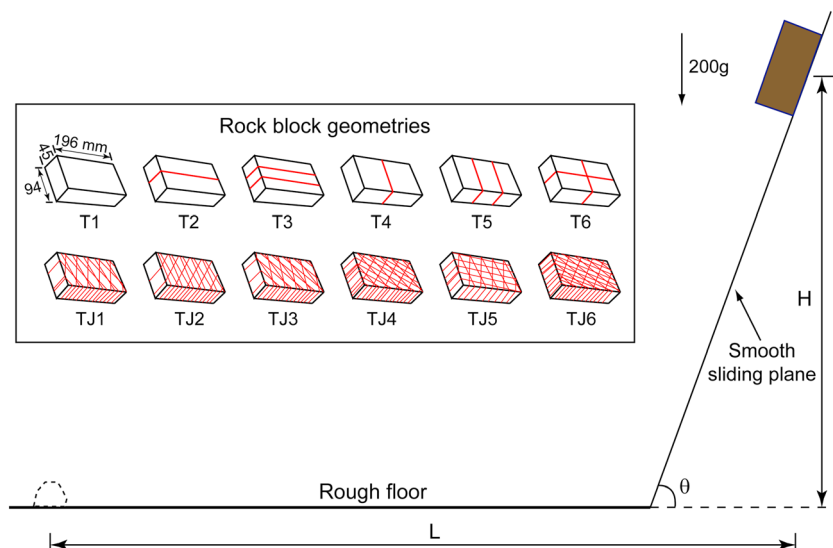










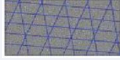
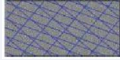


Figure 1. Geometry of the physical model adopted to investigate rock fragmentation in rock avalanches (θ is the slope angle. H is the initial block height. L is the runout distance measured as the boundary between 95% and 5% of the deposit mass). The inset plot shows the simulated geometries of the sliding rock block models. The series T1–T6 are intact and regular jointed rock blocks according to Bowman et al. (2012). TJ1–TJ6 are rock blocks with randomly distributed inclined joints, similar to those employed in Boon et al. (2015a).

Table 2
Numerical Configurations of Rock Blocks

Test	Note	Geometry	D_{ini}	Joint orientation	N	d
T1	Intact rock block		0	-	1	1
T2	Rock block with one transversal joint		0.038	0°E	2	0.794
T3	Rock block with two transversal joints		0.077	0°E-0°E	3	0.693
T4	Rock block with one longitudinal joint		0.019	90°E	2	0.794
T5	Rock block with two longitudinal joints		0.036	90°E-90°E	3	0.693
T6	Rock block with one transversal and one longitudinal joint		0.056	0°E-90°E	4	0.63
TJ1	Rock block with inclined joints		0.272	75°E-55°E-65°W	38	0.231
TJ2	Rock block with inclined joints		0.292	75°E-85°E-45°W	38	0.252
TJ3	Rock block with inclined joints		0.297	60°E-40°E-80°W	44	0.207
TJ4	Rock block with inclined joints		0.388	55°E-25°E-45°W	86	0.165
TJ5	Rock block with inclined joints		0.337	80°E-5°E-65°W	55	0.206
TJ6	Rock block with inclined joints		0.438	40°E-20°E-50°W	100	0.151

Note. For joint orientation, E = east; W = west. For example, 75°E = a 75° dip angle toward east. D_{ini} = initial damage ratio; N = initial number of fragments in a rock block; d = average fragment nominal size, $d = \sqrt[3]{V_f/V_0}$, with V_f being the volume of a fragment, and V_0 being the volume of a rock block prior to impact.

is larger than that used in Bowman et al. (2012) (maximum 50 g). This model configuration enables the generation of higher potential energy for modelling large rockslide and avalanche scenarios.

Here, the rock block is simulated as an assembly of 78,327 densely packed particles bonded together by breakable parallel bonds (Potyondy & Cundall, 2004) of assigned strength (see Table 1). The chosen granular packing porosity (n) is 0.41, and the total number of bonds for the intact rock block is 249,181. The jointed rock blocks with various internal subdivisions (joints) are illustrated in Figure 1 as inset plots, according to the experimental work in Bowman et al. (2012) and numerical analyses in Boon et al. (2015a). A more detailed description of the jointed rock configurations is given in Table 2. Although the simple regular joint geometries (e.g., series T1–T6 in Figure 1) can mimic the experimental configurations in Bowman et al. (2012), when applying such works to field studies, the question arises as to what extent the simplified models are representative of field conditions. In fact, the persistence, pattern and orientation of joints in real natural rock slopes are far more complicated than the regular geometries here adopted. Real natural jointed rock masses are usually sliced by more than two joint sets, making the failure patterns very complicated. Therefore, jointed rock masses consisting of three randomly selected and independent sets of joints were also investigated in this study (e.g., TJ1–TJ6 in Figure 1 and Table 2). These model configurations are employed to investigate the influence of rock discontinuity on the runout and fragmentation behavior of rock avalanches. The joints in a zone are here defined by debonding particles along the joint plane with a 3 mm thickness (\approx the mean particle diameter). As a result, a certain amount of debonded particles will be dispersed in the joint gaps, representing the gouge material in a real jointed rock mass. These dispersed particles interact with each other via

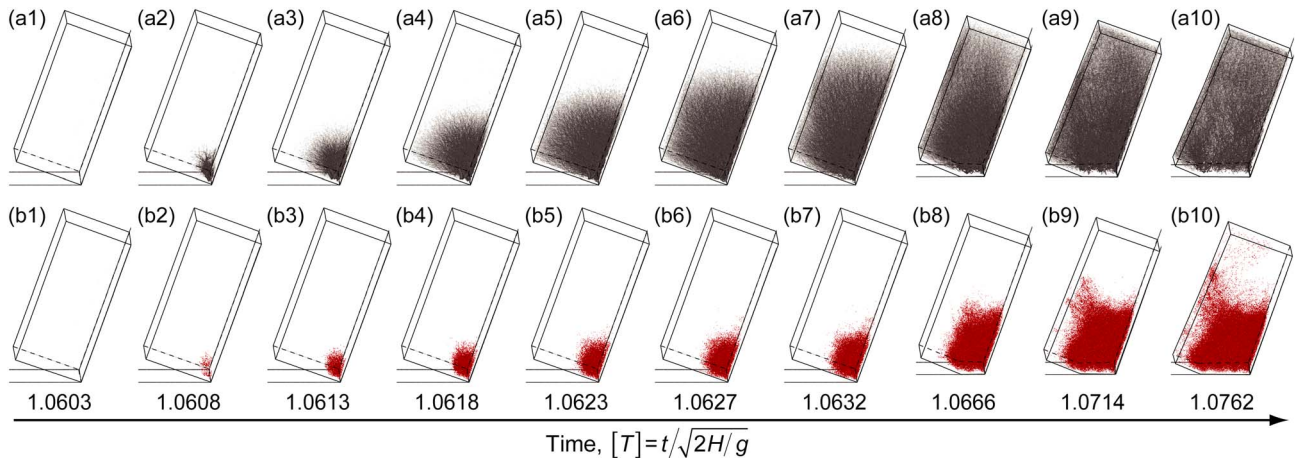


Figure 2. Evolution of force chains (series a: a1–a10) and bond breakages (series b: b1–b10) for an initial intact rock block (T1). The thickness of the chains is proportional to the force magnitude. In series b, a red dot is plotted where a bond breaks. The time interval between each figure in a1–a8 (b1–b8) is 10 μ s, while it is 100 μ s in a8–a10 (b8–b10).

the linear elastic spring-dashpot contact model. Here all joints are assumed to be fully persistent, so that they all slice the rock block completely. The numerical simulations were run on standard desktop computers (Intel® Core™ i7 CPU, 4.00 GHz \times 8, and 16 GB RAM) with each test costing around 35 hr.

3. Results

In the following analyses, nondimensional parameters will be employed in order to generalize the obtained numerical results to rock avalanches of different geometries.

3.1. Force Wave Propagation and Internal Rock Damage

In the current analyses, the force/bond chains of a granular assembly are defined as those presented in Zhao et al. (2017), with straight lines linking the particle centers representing the contact forces between the paired particles. The thickness of these lines is proportional to the force magnitude. According to De Blasio (2011), the evolution of force chains during a dynamic impact process can lead to the increase of impacting stresses and consequently increase the intensity of rock fragmentation. In Figure 2, it can be observed that at impact, the large contact forces and the corresponding internal damages arise immediately from the bottom frontal corner of the block (see Figures 2a and 2b). As the rock block collides onto and is sheared off along the bottom floor, the contact forces propagate radially upward very quickly to the block surface and upper rear region (see Figures 2a1–2a10) as a series of waves. However, very small impact-induced contact forces reach the upper rear region, without altering the integrity of the rock there (see Figure 2b10). Since the force chains carry most of the applied fracturing stresses (Makse et al., 2000), the localization of force chains at the bottom also increases the rock fragmentation intensity there. This conclusion is confirmed by observing the gradual enlargement of the areas of internal rock damage at the block bottom side (see Figures 2b1–2b10). The numerical simulation shows a pattern of fragmentation concentration near the impacting zone similar to the 2-D discrete element modelling of the fragmentation of a single circular particle reported in Potapov and Campbell (1994). Detailed descriptions of the evolution of internal rock damage within the rock block are provided in the supporting information.

The characteristics of force wave propagation (plotted as a sequence of wave front curves at fixed time steps) for the intact and jointed rock blocks (e.g., T1, T6, and TJ1 as in Figure 1) are illustrated in Figure 3. For the intact rock block (T1), the force wave propagates radially as a sequence of equally spaced arcs, indicating that the initial rock mass is homogeneous and isotropic. In this case, the speed of stress wave propagation is calculated as 1,316 m/s. The rock block with cross joints (T6) has a similar force wave propagation pattern as T1 but gradually reduced velocity in the lower half of the rock block (\approx 823.4 m/s). However, the transversal joint gap in the middle of the rock mass would lead to a 50 μ s time delay for the force wave to propagate from the lower to the upper part of the blocks. Due to the damping effect of

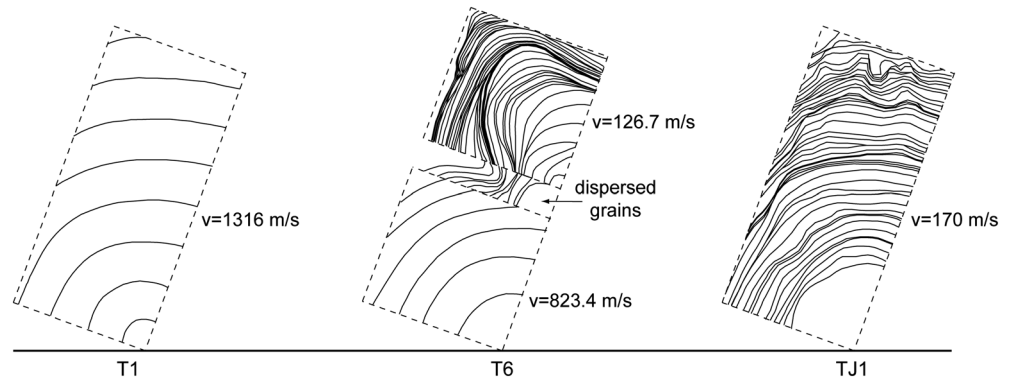


Figure 3. Position of force wave front within the rock block at different times. Each curve represents the force wave front with a force intensity value of 5 N. The force wave propagates from the bottom toe upward to the upper rear regions of the rock block. The dashed lines delimit the profile of rock block at impact. The time interval between each wave curve is 10 μ s. In T6, there is a 50- μ s delay time for the force wave travelling from the bottom to the upper rock.

dispersed grains in the joint gap, the force wave propagation in the upper rock block is very slow as shown by the closely distributed wave front curves. This phenomenon is consistent with the experimental observations in Sebastian and Sitharam (2016). As for the inclined jointed rock (TJ1), the force wave front curves are heavily distorted due to friction and damping in the interconnected joints. The general trend is that the force wave propagates radially upward at a very small velocity. The wave front distorts significantly as it approaches the upper surface where many small fragments exist and collide with the lower large blocks. The mean velocity of stress wave propagation is calculated as 170 m/s.

According to Figure 3, it is possible to estimate the velocity of the compressive force wave propagation (v_p) within an intact/jointed rock block for each test, as listed in Table 3. According to the table, the intact rock block has a relatively high force wave propagation velocity ($\approx 1,300$ m/s), while the inclined jointed rock blocks have very low bulk velocities (< 200 m/s). The lower section of the transversally jointed rock block also has a high velocity ($\approx 1,100$ m/s), while the upper sections have very low velocities (≈ 150 – 225 m/s) due to the friction and damping effects of joints. The force wave propagation velocity in longitudinally jointed rocks is smaller than that in an intact rock and decreases with the number of joints (see results for T4 and T5).

In the current DEM analyses, the estimated force wave velocity of an intact rock block ($\approx 1,300$ m/s) matches well the lower bound wave velocity of real coal rocks ($\approx 1,200$ to $2,500$ m/s for intact coal rocks under well-controlled testing conditions; see Krzesińska, 2000; Morcote et al., 2010; Wu et al., 2015). In addition, according to Pan et al. (2013), the compressive force wave velocity of rock, v_p , can be estimated by a theoretical equation:

$$v_p = \sqrt{\frac{E_b}{\rho_b} \frac{(1 - \nu)}{(1 + \nu)(1 - 2\nu)}} \quad (2)$$

where E_b and ρ_b are the bulk Young's modulus and density, respectively, and ν is the Poisson's ratio of coal rock. ρ_b can be computed from the sample porosity (n) and dry particle density (ρ_s) as

$$\rho_b = (1 - n)\rho_s \quad (3)$$

Thus, from equation (2) and the parameters listed in Table 1, v_p is calculated as 1,132 m/s, which is close to the numerical value of v_p for intact and regular jointed rock blocks obtained in this study. However, heavily prejointed rock blocks exhibit very low wave velocities (< 200 m/s).

Table 3
Force Wave Transmission Velocity (m/s) Within the Rock Block

Intact and regular joint		Inclined joint	
Test	Velocity (m/s)	Test	Velocity (m/s)
T1	1316.0	TJ1	170.0
T2	11,566.5 (b)	TJ2	196.8
T3	1,098.2 (b) 223.9 (m)	TJ3	167.0
T4	1,014.9	TJ4	142.4
T5	789.4	TJ5	173.6
T6	823.4 (b) 126.7 (u)	TJ6	155.5

Note. For transversally jointed rock block, the force wave velocity is different for each subdomain (b = bottom subdomain; m = middle subdomain; u = upper subdomain). See Figure 1 for the rock block geometry.

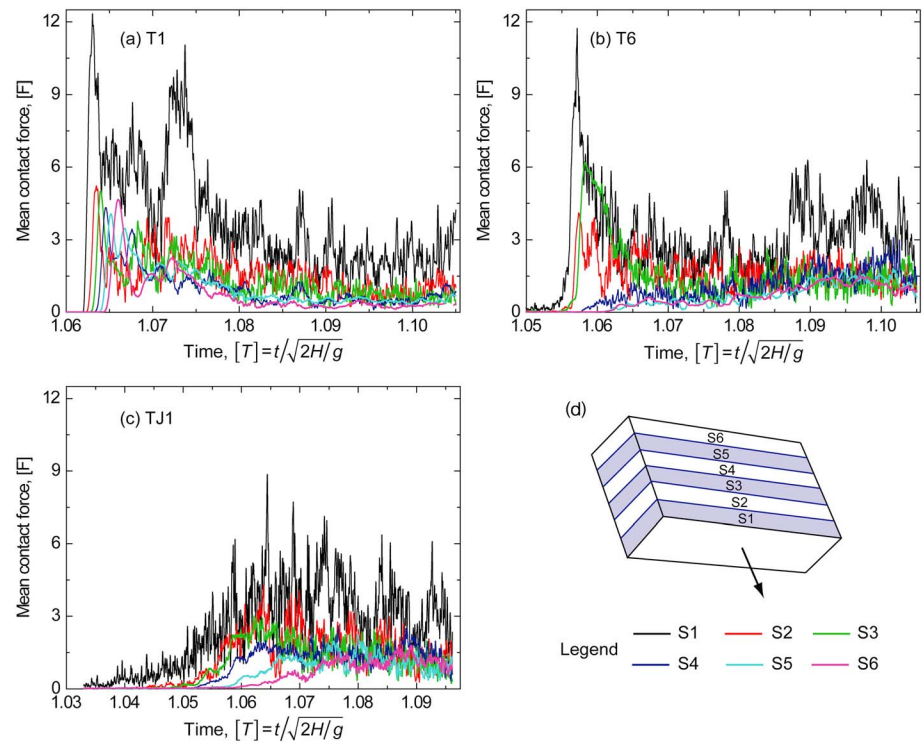


Figure 4. Evolution of mean interaction forces in each subdomain of the (a) intact (T1), (b) regular (T6), and (c) inclined (TJ1) jointed rock blocks. The block subdivision is shown in the inset plot in (d). S = subdomain; the mean contact force F_c is normalized as $[F] = F_c/G_0$, with G_0 being the mean gravity force of the particles in the rock block.

The corresponding evolution of contact forces within the rock block can also be analyzed for each test (here only T1, T6, and TJ1 are shown as representative tests. Results of the other tests can be found in the supporting information), as shown in Figure 4. In the current analyses, the rock block has been subdivided into six equidimensional subdomains along the longitudinal direction, with the index S1 to S6 representing the subdomains located from the bottom front to the upper rear regions (see the legend). The average properties of grains can be evaluated in each subdomain (the following analyses will use the same notation). From Figure 4, it emerges that the mean contact force within the rock block evolves as a series of waves. From the lower front to the upper rear subdomains, the peak contact force decreases slightly, due to frictional dissipation, plastic deformation, and the discontinuities within the granular matrix. However, the uppermost subdomain exhibits a slight increase of the peak contact force. This is because the downward inertial motion of the upper rock block can also generate force waves when it compresses the lower blocks. The superposition of upward and downward travelling force waves finally results in high peak contact forces. The bottom subdomains (S1 and S2) experience very intense fragmentation at impact, resulting in very strong oscillations of contact forces after the first impact of the block. The upper subdomains exhibit clear periods of damped force evolutions, such as reduced magnitudes (e.g., from 12 to 4) and enlarged periods (e.g., from 4×10^{-4} to 6×10^{-3}), indicating that the rockfall impact can indeed generate a series of transient elastic force waves, and the magnitudes of the subsequent waves decrease quickly due to intensive energy dissipation via friction and damping. The cross-jointed rock block (T6) shows apparent discontinuity of force wave transmission at the upper subdomains (e.g., S4, S5, and S6), such that the contact forces increase slowly and no peak force can be observed in the current time range. As for TJ1, the contact forces increase slowly, and their magnitude decreases progressively from the bottom to the upper subdomains. The increasing rate of contact force is much smaller than that observed in regularly jointed rock blocks (T1 and T6). In fact, the highly jointed rock structure effectively damps the granular dynamics and contact intensity.

3.2. Evolution of Rock Damage and Energy

The impact-induced fragmentation also involves energy transfers, which rule fragmentation intensity and fragment dynamics. As discussed in Zhao et al. (2017), the fragmentation intensity of rock varies under different testing conditions (e.g., loading strain rate and internal discontinuities), as reflected by the values of the damage ratio (D). The damage ratio of each subdomain of the rock block ($D^{(i)}$) is defined as the ratio of the number of broken bonds occurring during impact over the initial number of bonds in the subdomain (Thornton et al., 1996). The potential energy of each subdomain of the rock block is calculated as the summation of the potential energy of each particle, $E_p^{(i)} = \sum_{j=1}^{N_i} m_j g H_j$, with N_i being the number of particles in subdomain i , m_j and H_j being the mass and initial height of particle j . Before release, $E_p^{(i)}$ also corresponds to the total energy of the initial granular system ($E_0^{(i)}$) in subdomain i , while the summation $\sum_{i=1}^6 E_p^{(i)}$ corresponds to the initial potential energy of the whole rock block (E_0). The kinetic energy of each subdomain of the rock block is calculated as the summation of the translational and rotational kinetic energy of all particles in the subdomain, $E_k^{(i)} = \frac{1}{2} \sum_{j=1}^{N_i} (m_j |v_j|^2 + I_j |\omega_j|^2)$, with $I_j = 0.4 m_j r_j^2$ being the moment of inertia and v_j and ω_j being the translational and angular velocities of particle j . In addition, the elastic strain energy stored in each particle bond and contact are denoted as E_{bj} and E_{cj} , respectively, as in Zhao et al. (2017). At any time, the cumulative energy dissipated in each subdomain ($E_{diss}^{(i)}$) is calculated as

$$E_{diss}^{(i)} = E_0^{(i)} - E_p^{(i)} - E_k^{(i)} - \sum_{j=1}^{Nb_i} E_{bj} - \sum_{j=1}^{Nc_i} E_{cj} \quad (4)$$

where Nb_i and Nc_i are the number of bonds and contacts in subdomain i , respectively.

Figure 5a shows the evolution of the damage ratio ($D^{(i)}$) for each subdomain of the rock block. According to the plots, it is apparent that rock damage starts immediately after impact, and $D^{(i)}$ can reach a very large value in a short time (e.g., <1 ms). The increasing rate of $D^{(i)}$ becomes smaller going from subdomain S1 to S6 due to force wave transmission and energy dissipation. In all tests, the impact bears a significant influence on the frontal subdomains (S1, S2, and S3), and the damage ratio evolves in a similar way exhibiting very large final stable values ($D^{(i)} > 0.7$). In subdomain S1, the final damage ratio reaches 1, indicating that the rock in this region has been completely crushed during impact. However, $D^{(i)}$ reduces quickly to smaller than 0.4 in the upper rear subdomains (S5 and S6), because very small elastic stresses reach the upper rear subdomains to break the rock structure. This effect is particularly evident for test T1, so that the final damage ratios of subdomains S5 and S6 are almost the same and remain smaller than 0.1. Since the frontal resistance has been reduced significantly by fragmentation, the upper rock block is translated horizontally by the motion of dispersed grains, undergoing only a very small damage. For test T6, the presence of a transversal joint in the middle leads to an apparent time delay (2.5 ms) and decrease of $D^{(i)}$ in the upper three subdomains. The final stable damage ratio for S5 is negligibly small (<0.03), while it is around 0.15 for S6. This is because the collision of the upper block edge (S6) onto the ground during movement (rolling and sliding) can also cause high damages. The jointed rock (TJ1) exhibits a complete rock fragmentation at subdomain S1 but relatively smaller damage ratio for S2 and S3. This is because the jointed rock mass gets completely disintegrated at impact, reducing contact force transmission upward. As the rock damage ratio is closely related to rock fragmentation intensity, it is also possible to conclude that all the large fragments in the final solid deposits come from the upper subdomains (e.g., S5 and S6) with small $D^{(i)}$.

Figure 5b shows that the peak kinetic energy ($E_k^{(i)}$) is almost the same for all tests, while its subsequent evolution varies after the impact. It is apparent that after impact, the lower three subdomains (i.e., S1, S2, and S3) retain a large kinetic energy, which is associated with the long runout of fine fragments. On the contrary, the upper region of the rock block has very small kinetic energy, and thus the final runout distances of

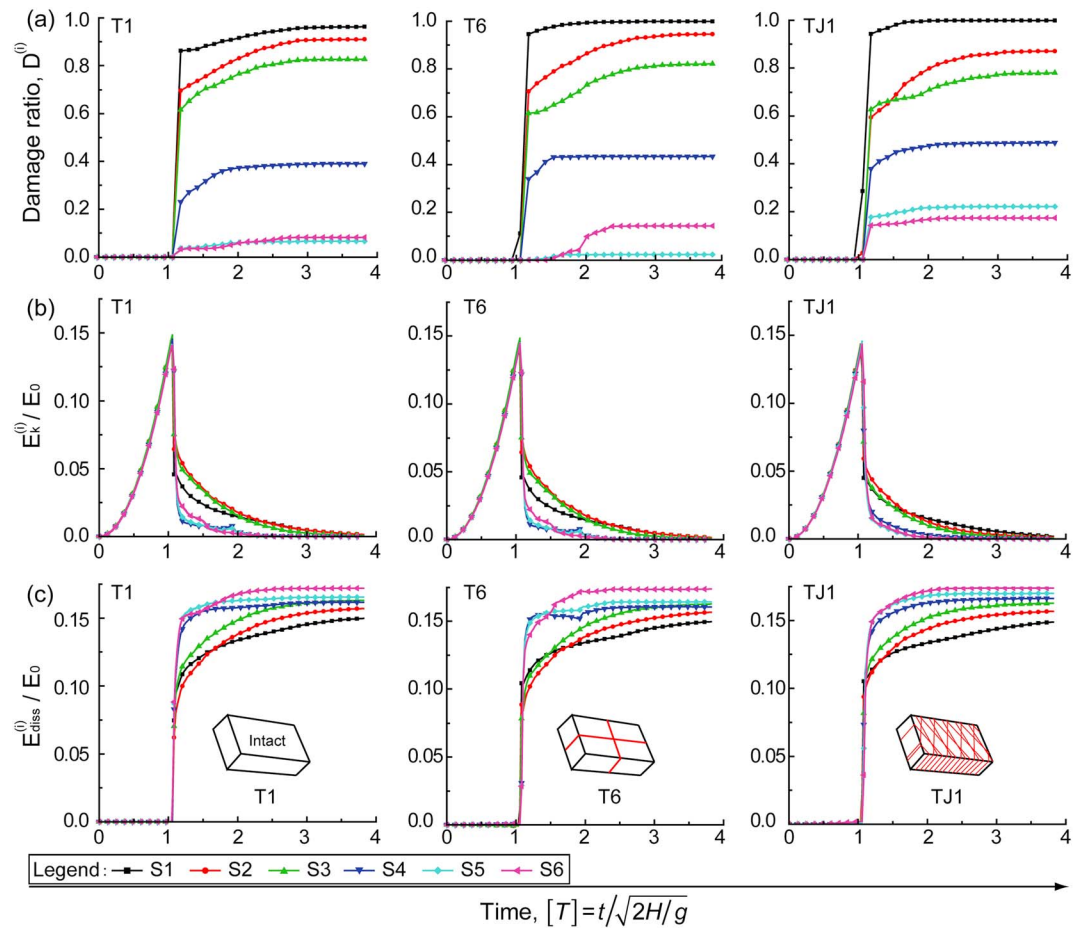


Figure 5. Evolution of (a) damage ratio ($D^{(i)}$) and (b) kinetic ($E_k^{(i)}$) and (c) dissipated ($E_{diss}^{(i)}$) energy in each subdomain of the intact (T1), regular (T6), and inclined (TJ1) jointed rock blocks. E_0 is the initial potential energy of the whole granular system.

coarse fragments are short. The upper two subdomains (i.e., S5 and S6) exhibit very small kinetic energy and evolve similarly, indicating that particles in the upper rear region are still bonded together. This feature can be explained by the fine fragments generated at the bottom which act as a cushion layer to effectively reduce the motion of the upper subdomains. Thus, the energy dissipated ($E_{diss}^{(i)}$) quickly increase from the bottom to the upper rock subdomains (see Figure 5c). In Figure 5c, it is also interesting to observe that shortly after impact, the dissipated energy of S1 is slightly larger than that of S2. The transient increase of $E_{diss}^{(i)}$ might result from intensive friction and damping that emerged at the sudden disintegration of the bottom layers. As for the upper subdomains (e.g., S5 and S6), the dissipated energy of S6 is smaller than that of S5 for a short period of time after impact, because the free boundary condition at the rear region allows the rebound of some fragments. However, the granular dynamics is damped quickly, and the subsequent interactions between fragments increase the energy dissipation in S6.

3.3. Fragment Distribution Characteristics and Size Spectrum

At the end of the simulation, the distribution of the granular deposits can be plotted in a plan view, as shown in Figures 6 and 9. For a better visualization, a set of distinct colors are used for different fragments (granular agglomerates consisting of more than 10 particles) and fragmented dispersed particles (light grey). Particles initially dispersed in the joint gaps are colored green. The initial locations of fragments and their sliding directions are plotted on the top of each figure. The overall damage ratio (D) of each rock block during impact is reported at the bottom. The cumulative mass distribution of the

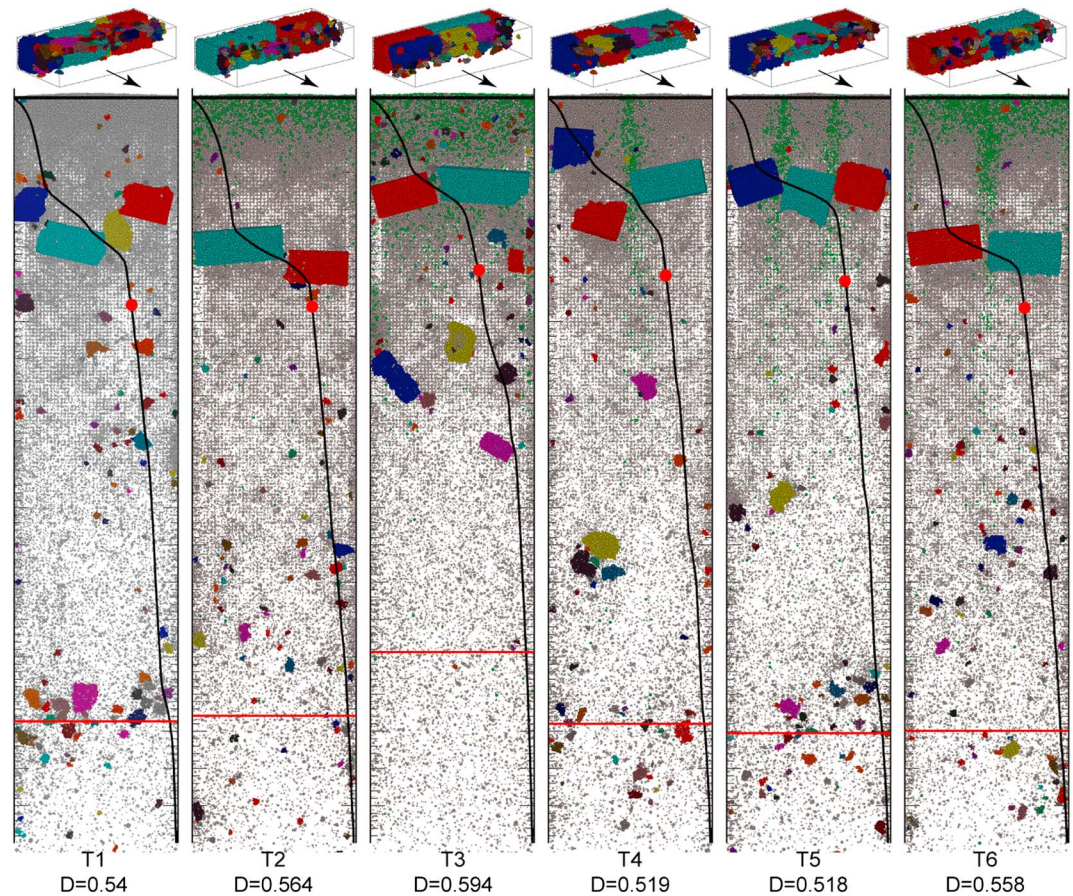


Figure 6. Plan view of the final granular deposits for simulations with regular joints (T1 to T6). The cumulative mass of the granular system along the path is plotted as black curves. Small images at the top show the relative position of the blocks generated at the impact. The value of damage ratio (D , defined as the ratio of the number of broken bonds to the total bonds of the initial rock block) for each test is labeled at the bottom of the figure. The green particles are originally dispersed in weak zones (joints). The mass center of the granular system is marked by a red dot, while the final runout distance (boundary of 95% granular mass) is marked by a horizontal red line.

rock along the path is plotted as a black curve together with its mass center (red dot on the curve). In the analyses, the spreading distance (L_C) of the granular mass center (measured from the slope toe) is

calculated as $L_C = \sum_{i=1}^N m_i l_i / M$ with M being the sum of the mass of all particles and l_i being the spreading

distance of particle i . The final fragment runout distance (L) is measured as the boundary between 95% and 5% of the deposit mass (i.e., 5% of the fragment mass is spreading ahead of the boundary; see the red lines plotted on the graphs). For all the tests, it is apparent that coarse fragments originating from the upper subdomains (S4, S5, and S6) have very short runout distance, while fine fragments from the lower subdomains (S1, S2, and S3) form the deposit front. The dispersed grains are mainly deposited near the slope toe region where they were first produced and then sheared off by the incoming upper blocks.

3.3.1. Tests on Regularly Jointed Rock Blocks

Figure 6 illustrates that for the intact rock block (T1), the final distribution of fragment size is well graded, due to the uniform impact force/stress wave transmissions within the rock (see Figure 3). For rock blocks with transversal joints (T2 and T3), a large number of very fine fragments are generated at the bottom frontal region, while only several large fragments originate from the upper block. These results indicate that a considerable amount of impact energy is absorbed by the bottom rock front, with complete disintegration of the rock structure and subsequent transportation of fine fragments far away. However, the middle and upper subdomains receive significantly less impact energy, which results in turn in a large

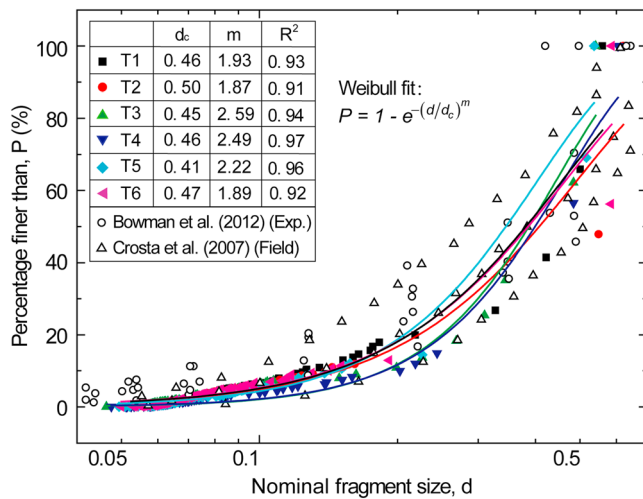


Figure 7. Fragment size distribution curves for test series T1–T6. Experimental and field observation data of the fragment size are normalized by the maximum fragment size reported in the corresponding publication. The fragment size distributions of each discrete element method test after the impact are fitted by the Weibull function, with the fitting parameters listed in the figure. The nominal fragment size of the numerical results is defined as $d = \sqrt[3]{V_f/V_0}$, with V_f being the volume of the fragment, and V_0 being the volume of the rock block prior to impact. In the Weibull fit, d_c is the characteristic particle size; R^2 is the adjusted coefficient of determination.

portion of medium and large sized fragments with much shorter run-out distance (see also the discussion about Figure 5). Tests T4 and T5 give rise to fragment size distribution patterns similar to T1, except that the size and shape of large fragments are significantly influenced by the initial joint distributions of the rock block. They also exhibit a more evident distribution of middle size clumps in the frontal part of the deposit. The fragment distribution pattern resulting from T6 could be described as a combination of T2 and T4, in which a large number of very fine fragments and several large fragments can be observed in the plot but with slightly longer runout distances for the large fragments.

The cumulative fragment size distributions (FSD) obtained from the current DEM tests are shown in Figure 7. In the analyses, the nominal fragment size is defined as $d = \sqrt[3]{V_f/V_0}$, with V_f being the volume of the largest fragment and V_0 being the volume of the rock block prior to impact. According to the figure, the FSD of intact and jointed rock block tests can be fitted well by a Weibull's distribution function ($R^2 \geq 0.91$), with very gentle and steep curvatures at the fine and coarse fragment size ranges, respectively. The only exception occurs at the very coarse fragment size range (e.g., nominal size of 0.5–0.6), where the mass percentage of the largest fragments exhibits a spike. The mismatch of fitting curves with the numerical data might stem from the dominant influence of initial joint orientations on determining the final fragment shapes. In this study, the numerical FSDs were also compared with the experimental results reported in Bowman et al. (2012) for impacts of jointed coal rocks (two or four blocks

arranged together, for the tests Frag 1-5, 1-6, 2-2, and 2-3 in their paper) in a centrifuge apparatus and the field observation data in Crosta et al. (2007). According to the comparison, it can be seen that even though testing method and model size scale are drastically different, the numerical results match experimental and field observations when normalized fragment sizes are employed.

As stated by Bulmer et al. (2005), Crosta et al. (2007), and Bowman and Take (2015), during rock avalanches, the fragment size decreases as a function of sliding distance, and a large amount of fine fragments can be transported to the distal ends. This phenomenon can also be visualized clearly looking at the final fragment deposition in Figure 6, while a quantitative study can be performed by plotting the FSDs along the deposition path. In our analyses, the final deposits were divided into four equal-sized (30 cm) regions with respect to the length of the horizontal channel (denoted as regions A, B, C, and D from the slope toe to the distal end; see also the inset plot), in which the FSDs of fragments were analyzed, as shown in Figure 8. It can be seen that more than 80% of solids in region A are very coarse fragments with a nominal diameter larger than 0.5, while also quite a few fine fragments ($d < 0.1$, $P < 10\%$) exist in this region. The mass of fine fragments is significantly larger in region B (Figure 8b). In particular, the nominal fragment sizes of deposits in tests T1, T2, and T6 are all smaller than 0.1. However, for tests T3 and T4, the majority of fragments ($P > 50\%$) are larger than 0.2. In regions C and D (Figures 8c and 8d), the FSD resulting from all tests (except T3) tend to be well graded, with the fragment size becoming gradually smaller (ranging from 0.05 to 0.2). In T3, only very few fine fragments exist at the distal ends, indicating that this joint structure is not efficient at debris transportation during rock avalanching.

3.3.2. Tests on Rock Blocks with Inclined Joints

The final fragment distribution characteristics of the rock blocks with inclined joints simulated in our DEM analyses are reported in Figure 9. It can be observed that the majority of rock fragments are deposited near the slope toe region, while only a small number of fine fragments reach the sliding front. The spreading distances of the granular mass centers (L_C , red dots in the plots) are approximately the same for tests TJ1–TJ6, which are shorter than that of an intact rock block. The final fragment runout distances (L , red lines in the plots) are also smaller than the distances for the regular jointed and intact rock blocks in Figure 6. In addition, the fragment distribution patterns are determined mainly by the

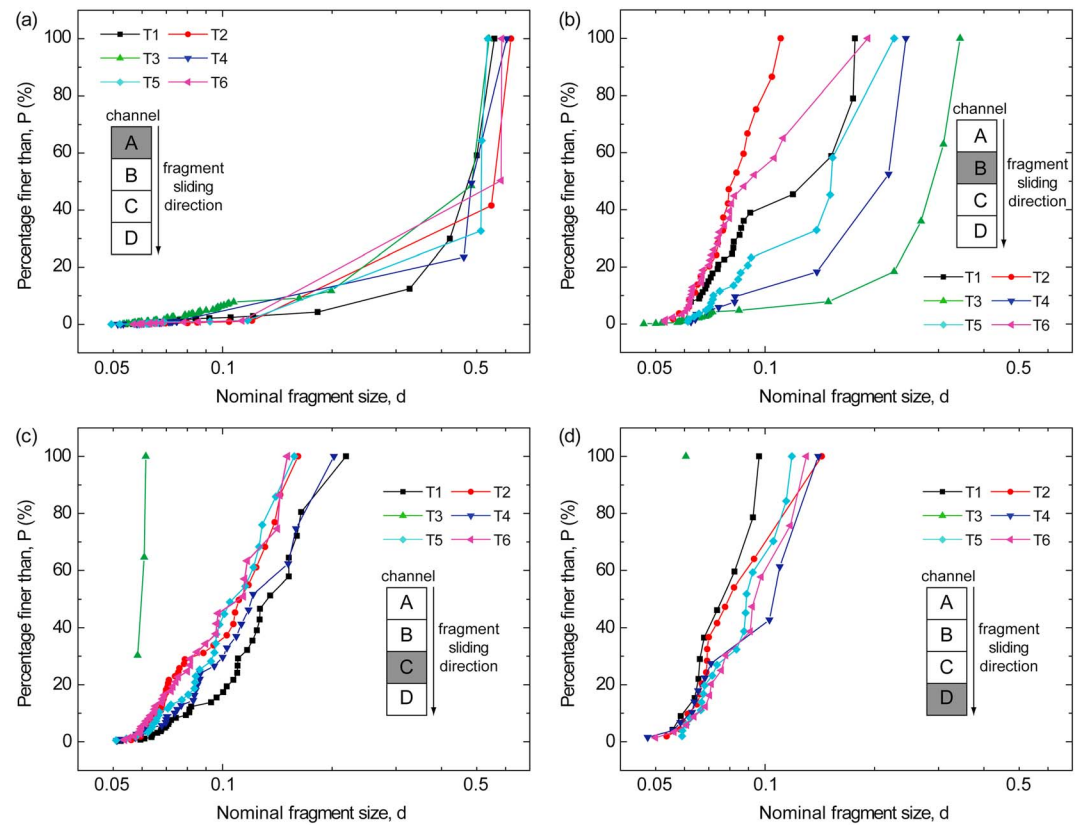


Figure 8. Fragment size distribution curves for debris materials resulted from regular jointed rock blocks at different locations along the horizontal channel. The studied region (length of 30 cm) is colored grey on the inset plot. (a) Region A. (b) Region B. (c) Region C. (d) Region D.

initial joint orientation and spacing and the fragmentation intensity. For rock blocks with steep joint orientations ($\geq 60^\circ$, with respect to the block bottom edge; e.g., TJ1 and TJ2), the impact can lead to a small rock damage ratio and a long fragment runout due to the large impulse contact force waves acting on the fine rock fragments. However, rock blocks with gentle joint orientations ($\leq 40^\circ$; e.g., TJ6) undergo much higher rock damage, because more particle bonds exist in the impacting region. From test TJ1 to TJ6, the cumulative granular mass curve becomes smoother, showing an increasingly uniform fragment grading.

Figure 10 illustrates the FSD results of inclined jointed rock blocks before (solid symbols) and after (hollowed symbols) impact. It can be seen that before impact, the jointed rock block consists of a large number of coarse fragments with varied sizes ($d > 0.2$, $P > 90\%$). After impact, a large number of fine fragments are produced, leading the FSD curve of each test to shift leftward to the fine size range ($d \leq 0.2$, $P > 40\%$). The final FSD of each test can be fitted well by a Weibull's distribution function. Figure 11 illustrates the final fragment size distribution along the horizontal channel. It can be observed that in region A, the FSD curves only shift slightly leftward from the initial ones (see Figure 11a), indicating a very low rock fragmentation intensity in this region. The coarse fragments with $d > 0.2$ amount to more than 60% of the solid mass. TJ3 undergoes the smallest damage such that the final FSD curve is very close to the initial one for $d > 0.33$. In regions B and C, the fragments become finer, and the maximum nominal fragment diameter (d_{\max}) approaches a unique value ($d_{\max} \approx 0.19$ in B and $d_{\max} \approx 0.125$ in C). However, TJ1 exhibits a drastically different grading pattern. It has a large number of fine fragments ($d < 0.07$, $P > 30\%$) and is poorly sorted for coarse fragments ($d > 0.11$) in region B, while several large fragments ($d > 0.1$, $P > 75\%$) are found in region C. Poor grading is exhibited in all tests in region D.

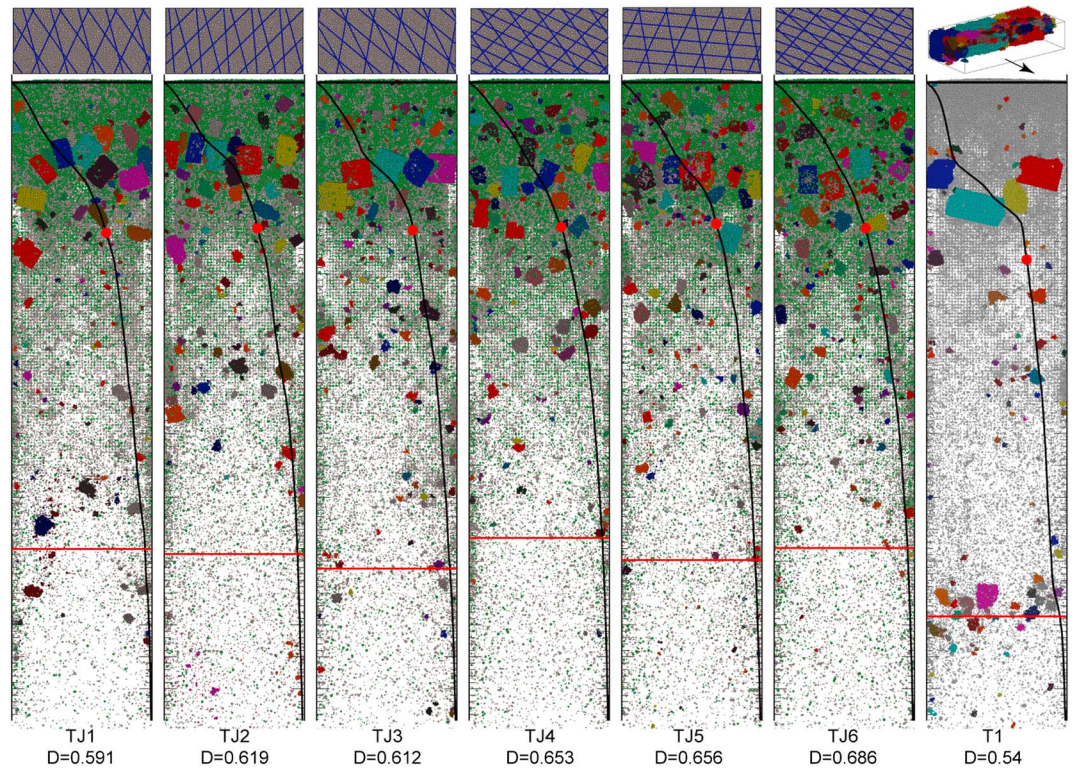


Figure 9. Plan view of the final granular deposits for tests on rock blocks with inclined joints. The cumulative mass of the granular system along the path is plotted as a black curve. Small images at the top show the initial joint configurations. The green particles are originally dispersed in the joint gaps. The mass center of the granular system is marked as a red dot, while the final runout distance (boundary of 95% granular mass) is marked as a horizontal red line.

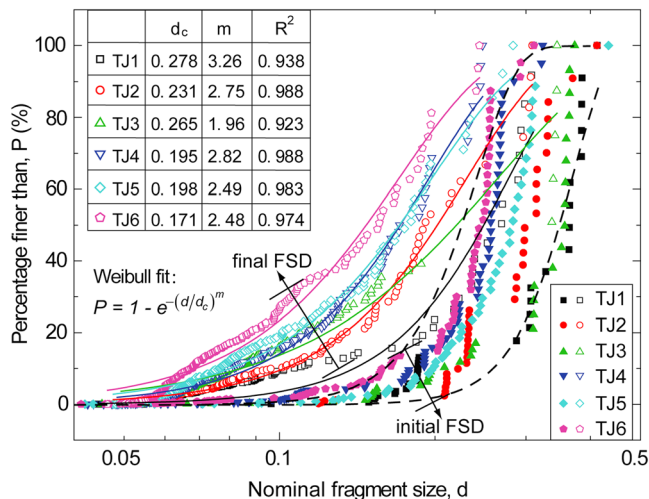


Figure 10. Fragment size distribution (FSD) curves for tests on rock blocks with inclined joints. The FSDs of each test after impact are represented by hollowed symbols and fitted by the Weibull function with the fitting parameters listed in the figure. The initial FSD data of rock blocks with inclined joints are represented by solid symbols and bounded by two Weibull distribution curves (black dashed curves). In the Weibull fit, d_c is the characteristic particle size; R^2 is the adjusted coefficient of determination.

4. Discussion

4.1. Momentum Boost Effect

According to De Blasio and Crosta (2015), the horizontal momentum (along the sliding direction) tends to increase suddenly after impact, so that some fine fragmented rock mass are ejected forward by the extra boosted momentum at high speeds. There is obviously no violation of momentum conservation law, because the extra horizontal momentum is taken up by the terrain at the slope break (Crosta et al., 2017). This effect may largely enhance the fragment runout distance and the resultant destructive power of a rock avalanche. Here, the momentum boost effect has been analyzed for all solids (i.e., dispersed grains and fragments; see Figure 12a) and pure fragments (see Figure 12b) in each subdomain of the rock blocks. Figure 12a shows that except for S4 in T6 and S6 in T1, a net momentum gain (boost) occurs for each subdomain in all tests. The subdomains undergoing very small or negative momentum gains at impact exhibit a very short runout distance for some large fragments (see also the discussion on Figure 5). Subdomain S2 undergoes the largest boosted momentum in each test, so that the produced fine fragments and dispersed grains in this region can travel long distances. As for subdomain S1, the sudden impact destructures the rock mass into dispersed grains with significantly constrained dynamics by the subsequent motion of the upper rock blocks. Thus, the momentum boost effect in this region is not significant. This result indicates that the two

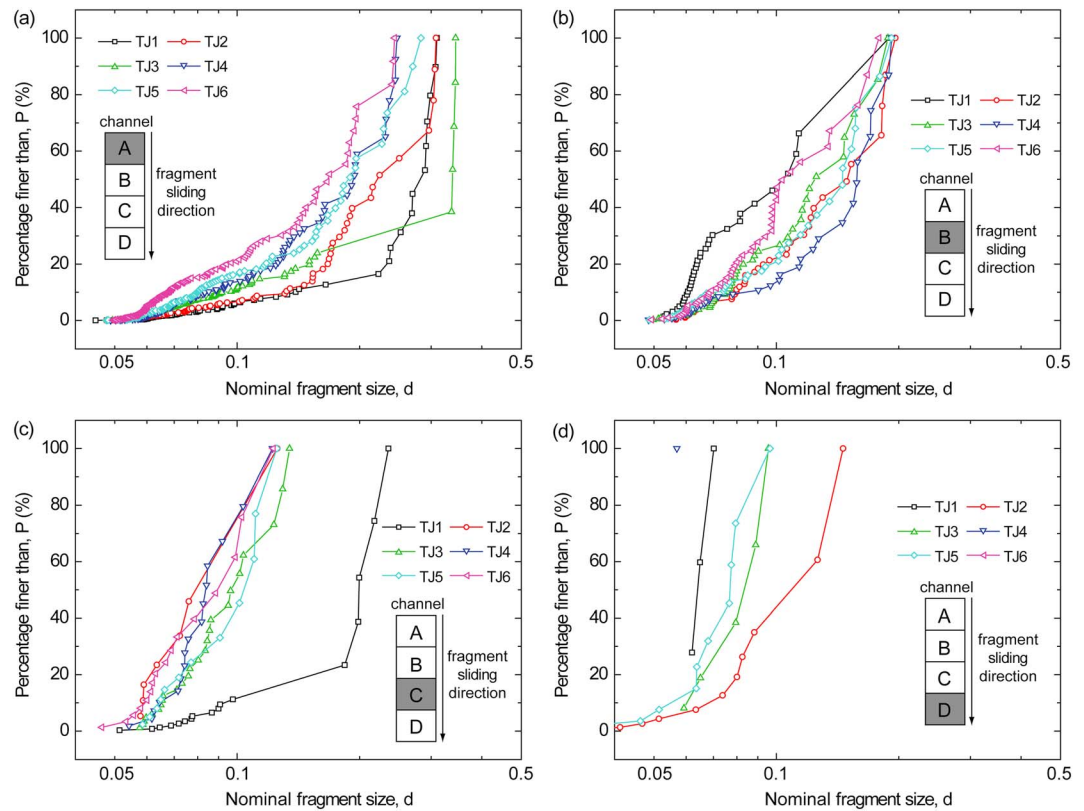


Figure 11. Fragment size distribution curves for debris materials resulted from rock blocks with inclined joints at different locations along the horizontal channel. The studied region (length of 30 cm) is colored grey on the inset plot. (a) Region A. (b) Region B. (c) Region C. (d) Region D.

frontal subdomains (S1 and S2) of a rock block can absorb the majority of impact energy, producing a large number of highly energetic fine fragments and dispersed grains. Among all tests, T1 exhibits the largest peak boosted momentum in subdomain S2.

According to the aforementioned findings, the momentum boost effect is not significant for dispersed grains due to intensive friction and damping effects. Thus, they can only travel very short distances. Since the major

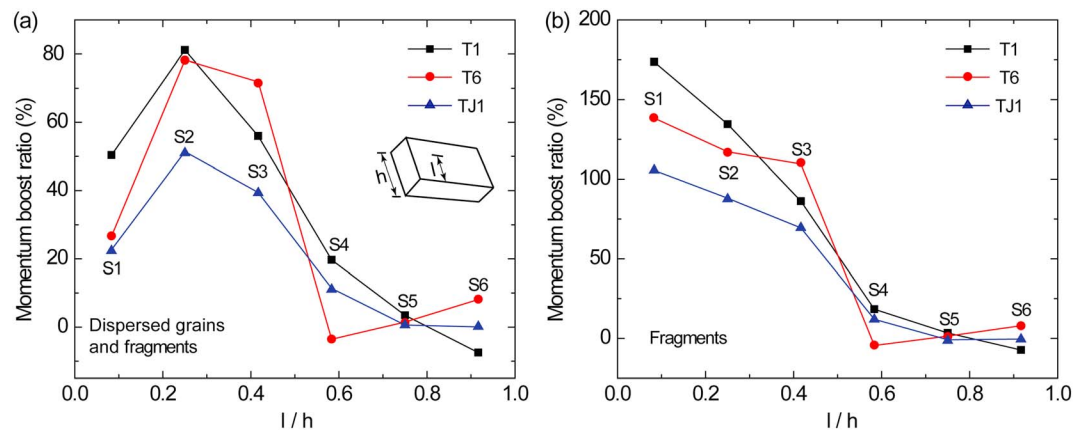


Figure 12. Momentum boost at impact for (a) all solids (dispersed grains and fragments) and (b) fragments (rock blocks consisting of at least 10 particles) in the model. The horizontal axis shows the relative position of each sublayer in the rock block, with l being the distance of the subdomain center to the block bottom edge, h being the height of the block sample. The subdivision of blocks in subdomains is the same as that discussed in Figure 4, and the index of each sublayer is labeled close to the data points.

Table 4
Percentage of Horizontal Momentum Boost for the Whole Granular System and Fragments (Unit: %)

Test	T1	T2	T3	T4	T5	T6	TJ1	TJ2	TJ3	TJ4	TJ5	TJ6
Dispersed particles and fragments	34.0	27.8	16.3	30.7	28.7	27.3	17.0	15.9	13.3	12.0	11.7	12.2
Fragments	17.3	11.2	13.6	12.7	11.9	11.9	15.0	12.0	8.0	14.0	12.9	14.5

Note. See also Figures 12a and 12b.

destructive power of rock avalanches comes from the highly energetic and far-reaching fragments, it is necessary to analyze the momentum boost effect of fragments in each subdomain, as shown in Figure 12b. It can be observed that the momentum boost ratio of fragments decreases sharply from the bottom frontal to the upper rear subdomains. The maximum momentum boost ratio of fragments occurs for subdomain S1. By comparing Figures 12a and 12b, it can be seen that the dispersed grains in S1 significantly reduce the momentum boost effect of the frontal subdomains. Even though small masses have very high potential of being ejected at impact, the intensive friction and constraints from neighboring masses can strongly reduce their motion. For TJ1, a large amount of dispersed grains can be produced after the impact due to the weak rock structure, reducing the overall momentum boost ratio in all subdomains significantly (see Figures 12a and 12b). The overall momentum boosts of the whole granular system and fragments for each test are listed in Table 4. The results show that the inclined jointed blocks (TJ series, heavily fragmented) tend to have smaller momentum boost of the whole granular system than the regular jointed blocks (T series). This is as expected, because the high friction and damping effects exist in the bulk solid deposits of heavily jointed rock blocks after impact. However, on average, they exhibit larger momentum boost of the fragments than the T series, because of the smaller size and higher mobility of each fragment. For tests on the T series, the low mobilized coarse fragments can reduce the overall momentum boost significantly. It should be noted that the momentum boost effect is significant for the frontal fine fragments, while it can be negligibly small or even negative for the large blocks at the tail. As a result, the majority of solid masses (large fragments) were deposited near the slope toe region (see Figures 6 and 9), as also observed experimentally in Bowman et al. (2012) and Bowman and Take (2015).

According to the discussions above, the fine fragments originating from the lower regions may have longer runout distances than the larger ones from the upper regions of the rock block (see Figure 5). This phenomenon indicates that fragments of various size (mass) maintain different kinetic energy after the impact, influencing the final runout distance. In the current analyses, the kinetic energy density of a specific fragment is defined as

$$[e] = \frac{\sum_{i=0}^{N_f} m_i |v_i|^2}{\left(gH \cdot \sum_{i=1}^{N_f} m_i \right)} \quad (5)$$

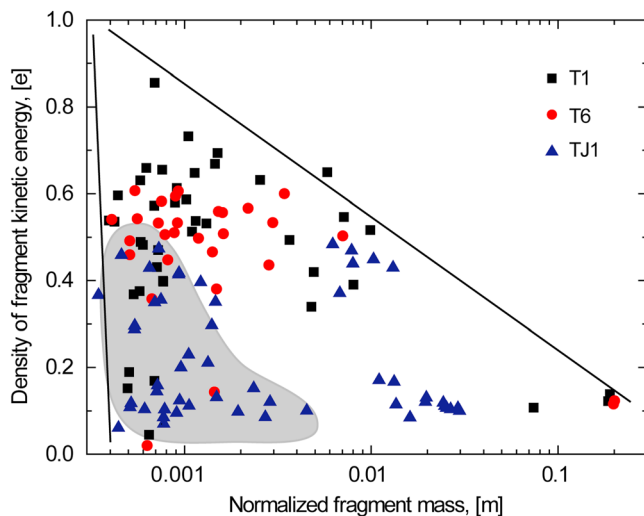


Figure 13. Energy density for different fragments. The fragment mass (m_i) is normalized by the mass of the initial rock block (M), as $[m] = m_i/M$.

where N_f is the total number of particles forming the fragment. Here only the translational velocity is considered in the calculation because it controls the final fragment runout distance.

Figure 13 shows the kinetic energy density of different fragments 2.5 ms after impact when the majority of fragments had been produced. The fine fragments normally exhibit very high kinetic energy, while the larger ones maintain very small energy (e.g., for $[m] > 0.02$, $[e]$ is smaller than 0.2). Even though there is some considerable scatter for these data points, the general trend holds true as indicated by the two regression lines on the graph. Since the small fragments can normally gain extra kinetic energy (momentum) at impact, they can run long distances (see also the discussions on Figures 6 and 9), as do some fly rocks during rockfalls and rock avalanches. These events are characterized by high velocity and low-angle trajectories. In the shaded area, the fine fragments exhibit very small kinetic energy density, because of either high energy dissipation (e.g., TJ1) or the barrier effect of large fragments

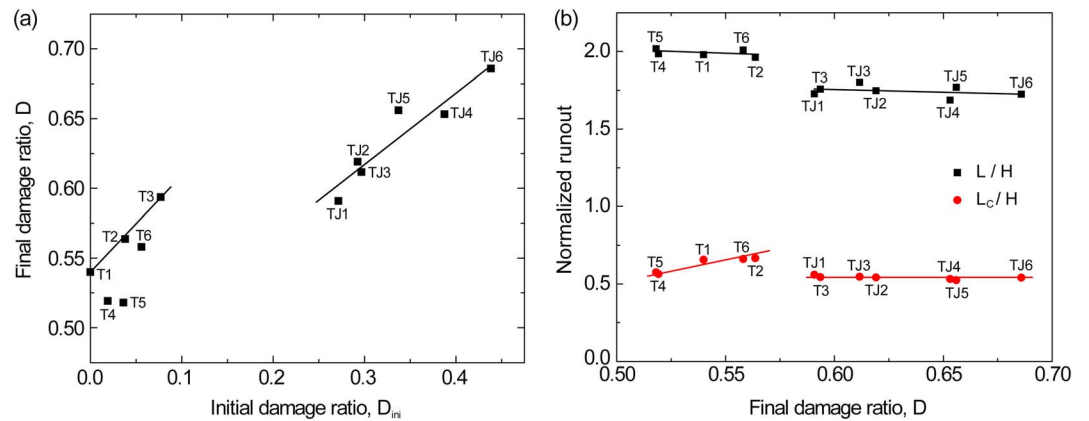


Figure 14. Modelling results for rock blocks with different initial joint configurations. (a) final damage ratio (D); (b) normalized runout distances.

(e.g., T1 and T6). In addition, under the current model configuration, the presence of lateral confinement can constrain the lateral motion of fragments, so that large fragments are mainly deposited near the slope toe region. However, in unconfined conditions fragments can spread laterally in a subcircular fan-like pattern, with shorter runout distances (Zhao et al., 2017).

4.2. Rock Damage Intensity and Avalanche Runout

The rock avalanche process involves intensive interactions between the rock mass and the ground/slope, leading to abrupt fragmentation at impact. Even though the first impact can be dominant, it should be noted that the subsequent impacts and collisions between fragments can also generate new force chains travelling within the fragmented rock blocks, leading to further crack propagations and rock damages (see Figure 5a). As stated by Bowman et al. (2012), the prejointed rock blocks may result in much lower damage intensity than the intact ones. This phenomenon is as expected because the jointed rock blocks with smaller individual block size can have much lower breakage potentials due to their high strength and integrated structure (Hardin, 1985). In addition, the natural coal rock blocks used in Bowman et al. (2012) experiments would inevitably contain some defects (e.g., microfractures or joints), and the probability of this kind of defects increases with block size. Therefore, analyses of rock fragmentation based on the fragment size distribution (see Bowman et al., 2012; Hardin, 1985) are not able to consider the disintegration of the internal microscopic rock structure with different initial block arrangements.

The current study attempted a detailed analyses of rock fragmentation using the so-called rock damage ratio (D , see the definition in section 3.2), which is also associated with the final runout distance (L_C and L). This parameter is useful for evaluating the potential destructive power of a rock avalanche event (Zhao et al., 2017). For rock blocks with preexisting joints (e.g., the regular and inclined joints), the initial debonding of particles within the joint gaps can be considered as the initial rock damage (D_{ini} , calculated as the ratio of the number of debonded to the initial number of bonds of an intact rock block). This parameter quantifies the initial damage intensity of a jointed rock mass. Figure 14a shows that the final rock damage ratio (D) increases with D_{ini} following approximately linear relationships. This trend indicates that jointed rock blocks are very susceptible to impact-induced fragmentation, because the stresses taken up per particle bond increases with D_{ini} ; that is, fewer bonds exist to resist the disintegration of the rock structure. For T2, T3, and T6, the alignment of individual rock fragments along the sliding direction causes the upper fragments to roll over the underlying ones after impact. Thus, the subsequent rapid sliding and collision of the upper fragments with the ground can lead to higher damage ratios than T1. This effect is particularly evident for tests on rock blocks with inclined joints where the fragments running towards the front get heavily crushed. However, T4 and T5 exhibit smaller final rock damage ratios than the other tests, indicating that rock blocks with longitudinal joints can effectively resist impact-induced fragmentation.

Figure 14b illustrates the normalized runout distances of the sliding front (L/H) and mass center (L_C/H) for various tests. In all tests, L/H decreases with D , following piecewise linear relationships. However, the

runout distance of the fragment mass center increases with D for both intact and regularly jointed rock blocks (T series), while it remains constant for rock blocks with inclined joints (TJ series). In general, the T series rock blocks show much longer runout distance than the TJ series rock blocks due to their high momentum boosts for fine fragments in the bottom subdomains (see the discussion about Figure 12). The only exception is for test T3 in which the fragment runout follows the same trend as TJ series tests exhibiting short fragment runout distances. It should be noted that the obtained numerical results are contrary to the generally accepted experimental and numerical results on intact rock masses in which the rock avalanche frontal runout distance (L) increases with the rock damage intensity (see Bowman et al., 2012; Bowman & Take, 2015; Zhao et al., 2017). The current study shows that the deposits of heavily jointed rock blocks can only spread over short distances, while the deposits of intact rock masses can reach the distal ends of the sliding path. The difference originates mainly from the way the runout distance is measured. In Bowman et al. (2012), an “interpreted length of runout” was defined to delimit the boundary between the bulk of solid material and the frontal saltating particles. This approach was reasonable in their experimental analyses because the bulk rock deposits were found close to the slope toe so the “true front” boundary can be easily identified. However, the identification of the runout length is somehow subjective, and it is not straightforward to estimate the destructive potential of a rock avalanche. In fact, the energy and momentum carried by a certain amount of granular mass at the sliding front are always of concern (Utili et al., 2015). Therefore, in this study, the fragment spreading distance defined as the boundary for 95% of granular mass can yield reasonably quantitative and consistent analyses among various simulations. In addition, from the numerical simulations, it emerges that the complete fragmentation of jointed rock blocks produces a thick layer of dispersed grains at the bottom which can to some extent lubricate the fragment motion but also significantly absorb a large portion of kinetic energy of the incoming rock fragments. Thus, the subsequent dynamic motion of large fragments is reduced significantly, resulting in short runout distances.

4.3. Model Size Effect

The small dimensions adopted in the present study allow to investigate the influence of rock block size on rock fragmentation. When applying the current work to field studies, the question arises about to what extent small-scale experiments/simulations are representative of field observations. In fact, many researchers have discussed the influence of model size on the mechanical response of a rock mass, and concluded that rock strength decreases with model size (Ayatollahi & Akbaridoost, 2014; Duan et al., 2007; Morel, 2008). In general, high-impact loading strain rates and fracturing stresses can be obtained from small rock samples (Bindiganavile & Banthia, 2006; Grady & Kipp, 1985; Zhang & Zhao, 2014). In this study, the numerical intact/jointed rock blocks considered have a maximum length of 0.196 m, which is significantly smaller than natural rock slopes (approximately 10–500 m). However, the use of augmented gravity and weak coal rock material in our numerical simulations ensure realistic stress and strain states for the simulated rock avalanche. In addition, the effect of frontal block fragmentation on the landslide deposit and its internal subdivision could help understand some of the large rockfall, rockslide, and rock avalanche deposits found in nature. Therefore, although simplified, the numerical model adopted provides meaningful insights into the fragmentation behavior of rock slopes, especially regarding some of the changes exhibited by solid microstructure and fragment dynamics during fragmentation.

5. Conclusions

This paper presents DEM investigations of the impact-induced fragmentation of jointed rock blocks during rockslide avalanches. In the DEM model, the intact rock blocks were generated by employing breakable parallel bonds to cement an assembly of densely packed spherical particles, while joints were generated by debonding particles in specific regions of the blocks. In this approach, the dynamic fragmentation and trajectories of rock blocks, such as internal force wave transmission, rock damage, energy dissipation, and fragment distribution characteristics, were captured successfully.

The sudden impact of a sliding rock block against an obstacle with a change in moving direction generates a series of force waves travelling radially from the bottom frontal to the upper rear regions of the rock block. The elastic force wave propagation velocity decreases with the initial joint frequency. In particular, rock blocks with inclined joints exhibit very small force wave propagation velocities (<200 m/s)

due to the damping effect of joints and an extremely weak solid structure. The large contact forces mainly concentrate at the bottom region generating a large number of fine fragments, while very small contact forces reach the upper part of the block producing several large fragments. In addition, the bottom frontal regions exhibit higher kinetic energy than the upper subdomains due to energy dissipation and momentum boost effect occurring at impact, leading to long runout distances for the fine fragments. For various tests, the final rock damage ratio increases, while the runout distance decreases with the increase of initial fragmentation intensity. The final fragment size distribution of intact and jointed rock blocks tends to be well graded, following a Weibull's distribution, and match well the experimental and field observations.

Acknowledgments

The data for this paper can be found in the supporting information. The authors would like to thank Elisabeth Bowman and one anonymous reviewer for their constructive comments that substantially improved this paper. This research was supported by the National Natural Science Foundation of China (grants 51639007 and 41602289), EU H2020 RISE grant "Geo-ramp" (grant 645665), and the @RockHoriZon advanced tools for rockfall hazard and risk zonation at the regional scale (grant 2016-0756), Fondazione CARIPL0. The Project MIUR-Dipartimenti di Eccellenza 2018-2022 is also thanked. Fabio De Blasio is acknowledged for his support.

References

- Agliardi, F., & Crosta, G. B. (2003). High resolution three-dimensional numerical modelling of rockfalls. *International Journal of Rock Mechanics and Mining Sciences*, 40(4), 455–471. [https://doi.org/10.1016/S1365-1609\(03\)00021-2](https://doi.org/10.1016/S1365-1609(03)00021-2)
- Alassi, H. T., & Holt, R. (2012). Relating discrete element method parameters to rock properties using classical and micropolar elasticity theories. *International Journal for Numerical and Analytical Methods in Geomechanics*, 36(10), 1350–1367. <https://doi.org/10.1002/nag.1056>
- Ayatollahi, M. R., & Akbaridoost, J. (2014). Size and geometry effects on rock fracture toughness: Mode I fracture. *Rock Mechanics and Rock Engineering*, 47(2), 677–687. <https://doi.org/10.1007/s00603-013-0430-7>
- Bindiganavile, V., & Banthia, N. (2006). Size effects and the dynamic response of plain concrete. *Journal of Materials in Civil Engineering*, 18(4), 485–491. [https://doi.org/10.1061/\(ASCE\)0899-1561\(2006\)18:4\(485\)](https://doi.org/10.1061/(ASCE)0899-1561(2006)18:4(485))
- Boon, C. W., Houlsby, G. T., & Ullari, S. (2014). New insights in the 1963 Vajont slide using 2D and 3D distinct element method analyses. *Geotechnique*, 64(10), 800–816.
- Boon, C. W., Houlsby, G. T., & Ullari, S. (2015a). Designing tunnel support in jointed rock masses via the DEM. *Rock Mechanics and Rock Engineering*, 48(2), 603–632. <https://doi.org/10.1007/s00603-014-0579-8>
- Boon, C. W., Houlsby, G. T., & Ullari, S. (2015b). A new rock slicing method based on linear programming. *Computers and Geotechnics*, 65, 12–29. <https://doi.org/10.1016/j.compgeo.2014.11.007>
- Bowman, E. T., & Take, W. A. (2015). The runout of chalk cliff collapses in England and France—Case studies and physical model experiments. *Landslides*, 12(2), 225–239. <https://doi.org/10.1007/s10346-014-0472-2>
- Bowman, E. T., Take, W. A., Rait, K. L., & Hann, C. (2012). Physical models of rock avalanche spreading behaviour with dynamic fragmentation. *Canadian Geotechnical Journal*, 49(4), 460–476. <https://doi.org/10.1139/t2012-007>
- Bulmer, M. H., Glaze, L. S., Anderson, S., & Shockey, K. M. (2005). Distinguishing between primary and secondary emplacement events of blocky volcanic deposits using rock size distributions. *Journal of Geophysical Research*, 110, B01201. <https://doi.org/10.1029/2003JB002841>
- Calvetti, F., Crosta, G., & Tatarella, M. (2000). Numerical simulation of dry granular flows: From the reproduction of small-scale experiments to the prediction of rock avalanches. *Rivista Italiana di Geotecnica*, 21(2), 21–38.
- Crosta, G. B., De Blasio, F. V., De Caro, M., Volpi, G., Imposimato, S., & Roddeman, D. (2017). Modes of propagation and deposition of granular flows onto an erodible substrate: Experimental, analytical, and numerical study. *Landslides*, 14(1), 47–68. <https://doi.org/10.1007/s10346-016-0697-3>
- Crosta, G. B., Frattini, P., & Fusi, N. (2007). Fragmentation in the Val Pola rock avalanche, Italian Alps. *Journal of Geophysical Research*, 112, F01006. <https://doi.org/10.1029/2005JF000455>
- Crosta, G. B., Imposimato, S., Roddeman, D., Chiesa, S., & Moia, F. (2005). Small fast-moving flow-like landslides in volcanic deposits: The 2001 Las Colinas landslide (El Salvador). *Engineering Geology*, 79(3–4), 185–214. <https://doi.org/10.1016/j.enggeo.2005.01.014>
- Cundall, P. A., & Strack, O. D. L. (1979). A discrete numerical model for granular assemblies. *Geotechnique*, 29(1), 47–65.
- Davies, T. R., & McSaveney, M. J. (1999). Runout of dry granular avalanches. *Canadian Geotechnical Journal*, 36(2), 313–320. <https://doi.org/10.1139/t98-108>
- De Blasio, F. V. (2011). Dynamical stress in force chains of granular media traveling on a bumpy terrain and the fragmentation of rock avalanches. *Acta Mechanica*, 221(3), 375–382. <https://doi.org/10.1007/s00707-011-0504-0>
- De Blasio, F., & Crosta, G. B. (2015). Fragmentation and boosting of rock falls and rock avalanches. *Geophysical Research Letters*, 42, 8463–8470. <https://doi.org/10.1002/2015GL064723>
- Duan, K., Hu, X., & Wittmann, F. H. (2007). Size effect on specific fracture energy of concrete. *Engineering Fracture Mechanics*, 74(1–2), 87–96. <https://doi.org/10.1016/j.engfracmech.2006.01.031>
- Dunning, S. A. (2006). The grain-size distribution of rock-avalanche deposits in valley-confined settings. *Italian Journal of Engineering Geology and Environment*, 1, 117–121.
- Erismann, T. H., & Abele, G. (2001). *Dynamics of rockslides and rockfalls*. Berlin: Springer.
- Fu, R., Hu, X., & Zhou, B. (2017). Discrete element modeling of crushable sands considering realistic particle shape effect. *Computers and Geotechnics*, 91, 179–191. <https://doi.org/10.1016/j.compgeo.2017.07.016>
- Giacomini, A., Buzzi, O., Renard, B., & Giani, G. P. (2009). Experimental studies on fragmentation of rock falls on impact with rock surfaces. *International Journal of Rock Mechanics and Mining Sciences*, 46(4), 708–715. <https://doi.org/10.1016/j.ijrmms.2008.09.007>
- Grady, D. E. (1981). Fragmentation of solids under impulsive stress loading. *Journal of Geophysical Research*, 86(B2), 1047–1054. <https://doi.org/10.1029/JB086ib02p01047>
- Grady, D. E., & Kipp, M. E. (1985). Mechanisms of dynamic fragmentation: Factors governing fragment size. *Mechanics of Materials*, 4(3), 311–320. [https://doi.org/10.1016/0167-6636\(85\)90028-6](https://doi.org/10.1016/0167-6636(85)90028-6)
- Hardin, B. O. (1985). Crushing of soil particles. *Journal of Geotechnical Engineering*, 111(10), 1177–1192. [https://doi.org/10.1061/\(ASCE\)0733-9410\(1985\)111:10\(1177\)](https://doi.org/10.1061/(ASCE)0733-9410(1985)111:10(1177))
- Haug, Ø. T., Rosenau, M., Leever, K., & Oncken, O. (2016). On the energy budgets of fragmenting rockfalls and rockslides: Insights from experiments. *Journal of Geophysical Research: Earth Surface*, 121, 1310–1327. <https://doi.org/10.1002/2014JF003406>
- Heim, A. (1882). Der Bergsturz von Elm. *Zeitschrift der Deutschen Geologischen Gesellschaft*, 34, 74–115.

- Hermanns, R. L., Blikra, L. H., Anda, E., Saintot, A., Dahle, H., Oppikofer, T., et al. (2013). Systematic mapping of large unstable rock slopes in Norway. In C. Margottini, P. Canuti, & K. Sassa (Eds.), *Landslide science and practice: Volume 1: Landslide inventory and susceptibility and hazard zoning* (pp. 29–34). Berlin: Springer.
- Imre, B., Laue, J., & Springman, S. (2010). Fractal fragmentation of rocks within sturzstroms: Insight derived from physical experiments within the ETH geotechnical drum centrifuge. *Granular Matter*, 12(3), 267–285. <https://doi.org/10.1007/s10035-009-0163-1>
- Jaeger, J. C. (1967). Failure of rocks under tensile conditions. *International Journal of Rock Mechanics and Mining Science and Geomechanics Abstracts*, 4(2), 219–227. [https://doi.org/10.1016/0148-9062\(67\)90046-0](https://doi.org/10.1016/0148-9062(67)90046-0)
- Jing, L., Kwok, C. Y., Leung, Y. F., & Sobral, Y. D. (2016). Characterization of base roughness for granular chute flows. *Physical Review E*, 94(5), 052901.
- Krzysińska, M. (2000). Correlation of absolute temperature coefficients of ultrasonic velocity in solutions of dilute coal and lignite extracts with molecular masses. *Fuel*, 79(15), 1907–1912. [https://doi.org/10.1016/S0016-2361\(00\)00051-X](https://doi.org/10.1016/S0016-2361(00)00051-X)
- Legros, F. (2002). The mobility of long-runout landslides. *Engineering Geology*, 63(3–4), 301–331. [https://doi.org/10.1016/S0013-7952\(01\)00090-4](https://doi.org/10.1016/S0013-7952(01)00090-4)
- Liu, X., Dai, F., Zhang, R., & Liu, J. (2015). Static and dynamic uniaxial compression tests on coal rock considering the bedding directivity. *Environmental Earth Sciences*, 73(10), 5933–5949. <https://doi.org/10.1007/s12665-015-4106-3>
- Locat, P., Couture, R., Leroueil, S., Locat, J., & Jaboyedoff, M. (2006). Fragmentation energy in rock avalanches. *Canadian Geotechnical Journal*, 43(8), 830–851. <https://doi.org/10.1139/t06-045>
- Makse, H. A., Johnson, D. L., & Schwartz, L. M. (2000). Packing of compressible granular materials. *Physical Review Letters*, 84(18), 4160–4163.
- Morcote, A., Mavko, G., & Prasad, M. (2010). Dynamic elastic properties of coal. *Geophysics*, 75(6), E227–E234.
- Morel, S. (2008). Size effect in quasibrittle fracture: Derivation of the energetic Size Effect Law from equivalent LFM and asymptotic analysis. *International Journal of Fracture*, 154(1), 15–26. <https://doi.org/10.1007/s10704-008-9291-6>
- Palmer, A. C., & Sanderson, T. J. O. (1991). Fractal crushing of ice and brittle solids. *Proceedings of the Royal Society of London. Series A: Mathematical and Physical Sciences*, 433(1889), 469–477. <https://doi.org/10.1098/rspa.1991.0060>
- Pan, J., Meng, Z., Hou, Q., Ju, Y., & Cao, Y. (2013). Coal strength and Young's modulus related to coal rank, compressional velocity and maceral composition. *Journal of Structural Geology*, 54, 129–135. <https://doi.org/10.1016/j.jsg.2013.07.008>
- Perinotto, H., Schneider, J. L., Bachèlery, P., Le Bourdonnec, F. X., Famin, V., & Michon, L. (2015). The extreme mobility of debris avalanches: A new model of transport mechanism. *Journal of Geophysical Research: Solid Earth*, 120, 8110–8119. <https://doi.org/10.1002/2015JB011994>
- Potapov, A. V., & Campbell, C. S. (1994). Computer simulation of impact-induced particle breakage. *Powder Technology*, 81(3), 207–216. [https://doi.org/10.1016/0032-5910\(94\)02907-5](https://doi.org/10.1016/0032-5910(94)02907-5)
- Potyondy, D. O., & Cundall, P. A. (2004). A bonded-particle model for rock. *International Journal of Rock Mechanics and Mining Sciences*, 41(8), 1329–1364. <https://doi.org/10.1016/j.ijrmmms.2004.09.011>
- Ruiz-Carulla, R., Corominas, J., & Mavrouli, O. (2017). A fractal fragmentation model for rockfalls. *Landslides*, 14(3), 875–889. <https://doi.org/10.1007/s10346-016-0773-8>
- Sammis, C. G., & Ben-Zion, Y. (2008). Mechanics of grain-size reduction in fault zones. *Journal of Geophysical Research*, 113, B02306. <https://doi.org/10.1029/2006JB004892>
- Scheidegger, A. E. (1973). On the prediction of the reach and velocity of catastrophic landslides. *Rock Mechanics*, 5(4), 231–236. <https://doi.org/10.1007/bf01301796>
- Sebastian, R., & Sitharam, T. G. (2016). Long-wavelength propagation of waves in jointed rocks—Study using resonant column experiments and model material. *Geomechanics and Geoengineering*, 11(4), 281–296. <https://doi.org/10.1080/17486025.2016.1139753>
- Shen, W. G., Zhao, T., Crosta, G. B., & Dai, F. (2017). Analysis of impact-induced rock fragmentation using a discrete element approach. *International Journal of Rock Mechanics and Mining Sciences*, 98, 33–38. <https://doi.org/10.1016/j.ijrmmms.2017.07.014>
- Stoopes, G. R., & Sheridan, M. F. (1992). Giant debris avalanches from the Colima Volcanic Complex, Mexico: Implications for long-runout landslides (>100 km) and hazard assessment. *Geology*, 20(4), 299–302.
- Strom, A. (2006). *Morphology and internal structure of rockslides and rock avalanches: Grounds and constraints for their modelling*. Paper presented at the Landslides from Massive Rock Slope Failure.
- Taboada, A., & Estrada, N. (2009). Rock-and-soil avalanches: Theory and simulation. *Journal of Geophysical Research*, 114, F03004. <https://doi.org/10.1029/2008JF001072>
- Thornton, C., Yin, K. K., & Adams, M. J. (1996). Numerical simulation of the impact fracture and fragmentation of agglomerates. *Journal of Physics D: Applied Physics*, 29(2), 424–435. <https://doi.org/10.1088/0022-3727/29/2/021>
- Timár, G., Kun, F., Carmona, H. A., & Herrmann, H. J. (2012). Scaling laws for impact fragmentation of spherical solids. *Physical Review E*, 86(1), 016113.
- Turcotte, D. L. (1986). Fractals and fragmentation. *Journal of Geophysical Research*, 91(B2), 1921–1926. <https://doi.org/10.1029/JB091iB02p01921>
- Utili, S., Zhao, T., & Houlsby, G. T. (2015). 3D DEM investigation of granular column collapse: Evaluation of debris motion and its destructive power. *Engineering Geology*, 186, 3–16. <https://doi.org/10.1016/j.enggeo.2014.08.018>
- Wang, Y. C., & Alonso-Marroquin, F. (2009). A finite deformation method for discrete modeling: Particle rotation and parameter calibration. *Granular Matter*, 11(5), 331–343. <https://doi.org/10.1007/s10035-009-0146-2>
- Weatherley, D., Boros, V., & Hancock, W. (2011). E5yS-particle tutorial and user's guide version 2.1. Brisbane: Earth Systems Science Computational Centre, The University of Queensland.
- Whitehouse, I. E., & Griffiths, G. A. (1983). Frequency and hazard of large rock avalanches in the central Southern Alps, New Zealand. *Geology*, 11(6), 331–334.
- Wu, H., Dong, S., Li, D., Huang, Y., & Qi, X. (2015). Experimental study on dynamic elastic parameters of coal samples. *International Journal of Mining Science and Technology*, 25(3), 447–452. <https://doi.org/10.1016/j.ijmst.2015.03.019>
- Xu, Y. (2005). Explanation of scaling phenomenon based on fractal fragmentation. *Mechanics Research Communications*, 32(2), 209–220. <https://doi.org/10.1016/j.mechrescom.2003.10.001>
- Zhang, Q. B., & Zhao, J. (2014). A review of dynamic experimental techniques and mechanical behaviour of rock materials. *Rock Mechanics and Rock Engineering*, 47(4), 1411–1478. <https://doi.org/10.1007/s00603-013-0463-y>
- Zhao, T., Crosta, G. B., Utili, S., & De Blasio, F. V. (2017). Investigation of rock fragmentation during rockfalls and rock avalanches via 3-D discrete element analyses. *Journal of Geophysical Research: Earth Surface*, 122, 678–695. <https://doi.org/10.1002/2016JF004060>

- Zhao, T., Houlby, G. T., & Uili, S. (2014). Investigation of granular batch sedimentation via DEM-CFD coupling. *Granular Matter*, *16*(6), 921–932.
- Zhao, T., Uili, S., & Crosta, G. B. (2016). Rockslide and impulse wave modelling in the Vajont Reservoir by DEM-CFD analyses. *Rock Mechanics and Rock Engineering*, *49*(6), 2437–2456. <https://doi.org/10.1007/s00603-015-0731-0>
- Zhou, J. W., Cui, P., & Fang, H. (2013). Dynamic process analysis for the formation of Yangjiagou landslide-dammed lake triggered by the Wenchuan earthquake, China. *Landslides*, *10*(3), 331–342. <https://doi.org/10.1007/s10346-013-0387-3>